A portable NIR fluorimeter directly quantifies singlet oxygen generated by nanostructures for Photodynamic Therapy

Spectrochimica Acta Part A: Molecular and Biomolecular Spectroscopy

A portable NIR spectrometer directly quantifies singlet oxygen generated by nanostructures for Photodynamic Therapy.

--Manuscript Draft--

Manuscript Number:	
Article Type:	Full Length Article
Section/Category:	Analytical Spectroscopy and New Methods
Keywords:	Photodynamic Therapy; Singlet Oxygen detection; NIR spectroscopy; Nanomedicine; Radiotherapy
Corresponding Author:	Luigi Cristofolini, Associate Professor University of Parma, Italy PARMA, ITALY
First Author:	Davide Orsi, Ph D
Order of Authors:	Davide Orsi, Ph D
	Vaccari Marco
	Baraldi Andrea, Associate Professor
	Luigi Cristofolini, Associate Professor
Abstract:	This paper reports on the setting up and calibration of a portable NIR spectrometer specifically developed for quantitative direct detection of the highly reactive singlet oxygen chemical specie, of great importance in Photodynamic therapies. This quantification relies on the measurement of fluorescence emission of singlet oxygen, which is peaked in the near-infrared (NIR) at λ= 1270nm In recent years, several nanostructures capable of generating reactive oxygen species (ROS) when activated by penetrating radiation (X-rays, NIR light) have been developed to apply Photodynamic Therapy (PDT) to tumours in deep tissue, where visible light cannot penetrate. A bottleneck in the characterization of these nanostructures is the lack of a fast and reliable technique to quantitatively assess their performances in generating ROS, and in particular singlet oxygen . For instance, the widely used PDT “Singlet Oxygen Sensor Green” kit suffers from self-activation under X-ray irradiation. To solve this difficulty, we propose here direct detection of singlet oxygen by a spectroscopic technique, thanks to recently developed thermoelectrically cooled InGaAs single photon avalanche photodiodes (SPAD). We couple an InGaAs SPAD to a custom-made integrating sphere. After calibrations on standard photosensitizers, we demonstrate the potentiality of this instrument characterizing some photosensitizing nanostructures developed by us. We also determine the detection threshold for our apparatus, which turns to be of the order of 4*10^9 singlet oxygen molecules in realistic experimental condition and for measurements extending to 1 minute of integration.
Suggested Reviewers:	Jean-Marie Aubry Universite de Lille Jean-Marie.Aubry@univ-lille.fr expert in singlet oxygen production and detection
	Sandhya Clement s.clement@unsw.edu.au expert in the field

UNIVERSITÀ
DI PARMA

DIPARTIMENTO DI SCIENZE
MATEMATICHE, FISICHE
E INFORMATICHE

Parco Area delle Scienze 7/A , 43124 PARMA

Parma, 12/04/2021

To the Editor of Spectrochimica Acta A,

On behalf of all the authors, I would like to submit to your attention the paper "A portable NIR spectrometer directly quantifies singlet oxygen generated by nanostructures for Photodynamic Therapy" by D. Orsi, M. Vaccari, A. Baraldi and L. Cristofolini.

We believe this paper is of interest to the readership of "Spectrochimica Acta A" because it reports on a new portable NIR spectrometer developed for direct detection of the highly reactive singlet oxygen ($^1O_2$) chemical specie, of great importance in Photodynamic therapies (PDT). The instrument is specifically designed for the investigation of nanostructures for Self-Lighted Photodynamic Therapy (i.e. PDT excited by penetrating radiation, such as X-rays generated from Radiotherapy sources of clinical use). The NIR emission from $^1O_2$ is collected by a custom-made integrating sphere coupled to an InGaAs Single Photon Avalanche Diode (SPAD). After calibrations on standard photosensitizers, we demonstrate the potentiality of this instrument in characterizing photosensitizing nanostructures. We also determine the detection threshold for our apparatus, which turns to be $\sim 4 \cdot 10^9$ $^1O_2$ for measurements extending to 1 min integration time in realistic experimental conditions.

Looking forward for your decision, I thank you for your kind attention and I send you my best regards.

Yours sincerely

On behalf of all the authors,

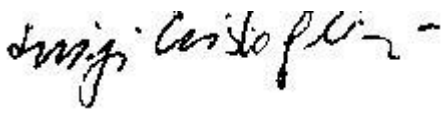

Luigi Cristofolini
Associate professor
Department of Mathematical, Physical and Computer Sciences,
University of Parma

Graphical abstract

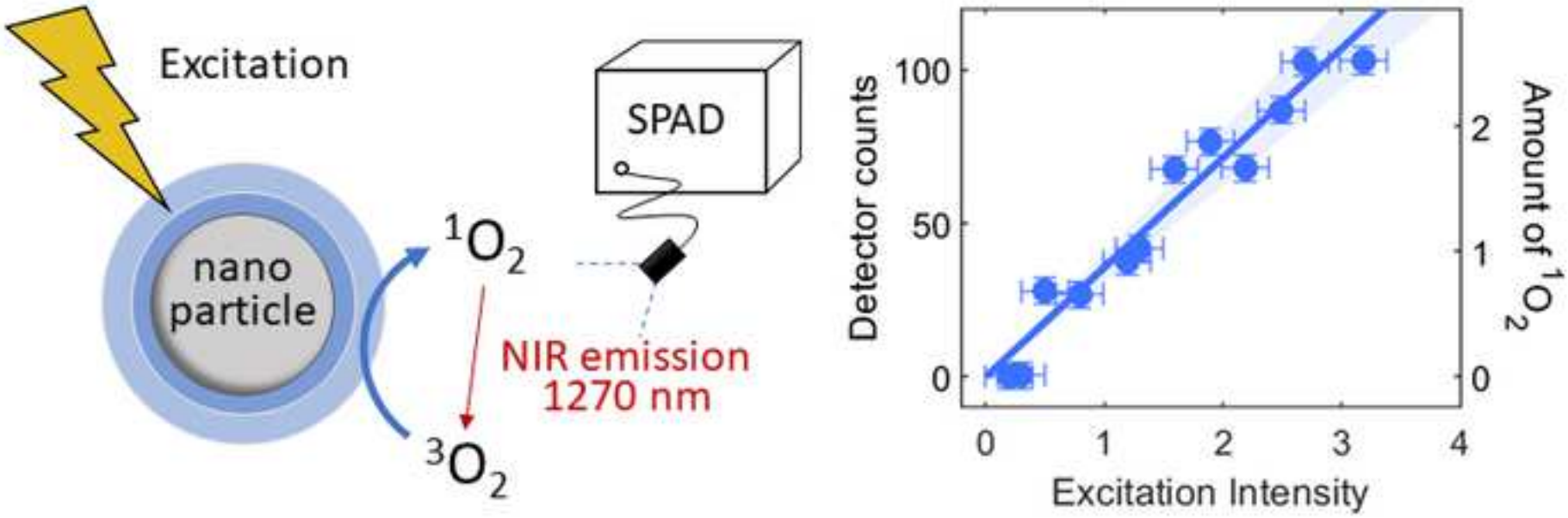

A portable NIR spectrometer directly quantifies singlet oxygen generated by nanostructures for Photodynamic Therapy.

Orsi Davide[1*], Vaccari Marco[1], Baraldi Andrea[1], Cristofolini Luigi[1†]

[1] - Università di Parma, Dipartimento di Scienze Matematiche, Fisiche e Informatiche, Parma (IT)

Abstract

This paper reports on the setting up and calibration of a portable NIR spectrometer specifically developed for quantitative direct detection of the highly reactive singlet oxygen ($^1O_2$) chemical specie, of great importance in Photodynamic therapies. This quantification relies on the measurement of fluorescence emission of $^1O_2$, which is peaked in the near-infrared (NIR) at $\lambda = 1270\ nm$.

In recent years, several nanostructures capable of generating reactive oxygen species (ROS) when activated by penetrating radiation (X-rays, NIR light) have been developed to apply Photodynamic Therapy (PDT) to tumours in deep tissue, where visible light cannot penetrate. A bottleneck in the characterization of these nanostructures is the lack of a fast and reliable technique to quantitatively assess their performances in generating ROS, and in particular $^1O_2$. For instance, the widely used PDT "Singlet Oxygen Sensor Green" kit suffers from self-activation under X-ray irradiation.

To solve this difficulty, we propose here direct detection of $^1O_2$ by a spectroscopic technique, thanks to recently developed thermoelectrically cooled InGaAs single photon avalanche photodiodes (SPAD).

We couple an InGaAs SPAD to a custom-made integrating sphere. After calibrations on standard photosensitizers, we demonstrate the potentiality of this instrument characterizing some photosensitizing nanostructures developed by us. We also determine the detection threshold for our apparatus, which turns to be $\sim 4 \cdot 10^9$ $^1O_2$ in realistic experimental condition and for measurements extending to 1 minute of integration.

Keyword. Photodynamic Therapy, Singlet Oxygen detection, NIR spectroscopy, Nanomedicine, Radiotherapy

* davide.orsi@unipr.it
† luigi.cristofolini@unipr.it

1. Introduction

Photodynamic Therapy is routinely used for the treatment of superficial tumours, in particular of the skin; it is based on the generation of reactive oxygen species (ROS) by photosensitizer (PS) molecules or nanostructures upon irradiation with light. Cancer cells are typically characterized by high metabolic ROS levels, which stress their scavenging mechanisms [1]; therefore, they are more susceptible than healthy cells to additional ROS photogenerated by a PDT agent [2,3].

The photogeneration of ROS from molecular PDT agents is categorized into Type I or Type II pathways [4,5]. Type I are complex pathways involving an electron or proton exchange between the PS triplet excited state and a substrate (e.g. the cell membrane, water, oxygen, or another molecule) leading to the formation of ROS, typically superoxide, hydrogen peroxide and hydroxyl radicals [5]. Type II photogeneration involves a direct energy transfer from the PS triplet excited state to molecular oxygen in its triplet state, yielding singlet oxygen ($^1O_2$) [4,5]. Superoxide and hydroxyl radicals generated by Type I routes can also reacts with each other, producing additional $^1O_2$.

Typically, molecules with efficient Type II pathways and high $^1O_2$ yields are selected as PDT agents [6,7]; the precise quantification of their performance in $^1O_2$ generation is a fundamental step in their characterization. The use of molecular probes is a widely used ROS detection strategy, because of its simplicity of use and low cost [8,9]. Particularly useful are chemofluorescent probes selective for specific ROS, such as the commercially available Singlet Oxygen Sensor Green (SOSG kit, Molecular Probes Inc.), a fluorescein derivative functionalized with an anthracene-derived moiety that quenches its fluorescence emission. In presence of $^1O_2$, this moiety is converted in endoperoxide anthracene, and the fluorescence emission of fluorescein is restored [10]. Accordingly, SOSG is advertised as a selective and quantitative probe for $^1O_2$, and proficiently and widely used in recent years [8,11].

Chemofluorescent probes such as SOSG have been used to measure $^1O_2$ from nanostructures developed to overcome the main limitation of standard PDT, i.e. the low penetration of visible light in tissues. These nanostructures exploits nanomaterials capable of absorbing highly penetrating radiation, such as near-infrared photons [12–16] or high-energy X-rays [17–19], and excite a PS coupled to them, enabling triggered ROS generation in cancer cells located in deep tissues, where visible light cannot reach. In the case of nanostructures for PDT activated by X-rays, the therapy is named Self-Lighted Photodynamic Therapy (SLPDT) or X-ray Photodynamic Therapy (XPDT). SOSG, for instance, has been used to characterize porphyrin-functionalized SiC-SiO_2 nanowires for XPDT, measuring $^1O_2$ generation as a function of the X-ray dose built up in the sample; irradiation was provided by a clinical 6 MeV Radiotherapy linear accelerator [20]. This experiment, however, requires careful calibration and background measurements to account for a series of undesired effects connected to the use of SOSG:

- The anthracene moiety, after reaction $^1O_2$, becomes itself a PS under irradiation with UV light, generating $^1O_2$ and thus corrupting the direct proportionality with SOSG fluorescence emission intensity [21];
- SOSG can be activated in absence of $^1O_2$ when irradiated by γ-rays from a cobalt-60 source ($1.17 - 1.33\ MeV$) or by X-rays ($320\ keV$) [22].

An attracting alternative is the direct detection of the fluorescence emission of $^1O_2$ peaked at $1270\ nm$, by using a near-infrared (NIR) spectrometer. This is made difficult by the low intensity of this emission, as discussed in section 2, and because of the lower performances of NIR detectors with respect to those in the UV-vis range in terms of signal-to-noise ratio and dark current. Several commercial NIR spectrometers for direct $^1O_2$ detection from PDT photosensitizers activated by visible light are available; these instruments, however, are not readily usable to characterize nanostructures for NIR/X-ray PDT, as they lack an portability

and adaptability to address the technical challenges posed in particular by X-ray sources. For instance, in the case of X-ray PDT nanostructures to be irradiated by clinical Radiotherapy linear accelerators operating in the MeV range, these difficulties must be considered:

- In Radiotherapy, the dose released in the tissue is mainly due to a cascade of secondary particles triggered by the transit of high-energy X-rays photons within the tissue itself, or within water-equivalent materials placed for this purpose; any electronic equipment in the proximity of the X-ray beam must be heavily shielded, to avoid severe problems with electronic noise;
- the need for a custom-made sample environment and light collection optics that does not shield the sample from incoming radiation;
- the instrumentation must be compact, transportable, and easily installable; any Radiotherapy LINAC is primarily used for treatment of cancer patients, and limited time and space is available for material science investigations.

These limitations define current state-of-the-art experiments. For instance, in ref. [23] the performance of porphyrin-grafted Tb_2O_3 scintillating NP were characterized by combining a) NIR spectroscopy to detect $^1O_2$ generated under visible light matching the scintillating emission of Tb_2O_3 NP, with b) X-ray emission spectroscopy under irradiation with a laboratory X-ray source and with c) SOSG $^1O_2$ detection under X-ray irradiation. Experiment a) was performed with a commercial, modular Horiba Jobin Yvon Fluorolog-3 spectrofluorimeter; this instrument and other analogous state-of-the-art laboratory instruments (i.e. from Edinburgh Instruments) lacks portability and are limited to excitation in the UV-Vis range. In experiment b), a UV-Vis spectrometer is used in conjunction with a laboratory X-ray source at 44 keV; this wavelength lies very far from the MeV wavelength range of photons used in Radiotherapy, hence the photon-matter interactions that leads to the build-up of the dose in the sample, to XEOL excitation and finally to $^1O_2$ generation are radically different. The combination of these a-b-c experiments can provide a detailed, yet indirect and incomplete picture of the nanostructure performances.

This paper proposes a transportable, fiber-optic coupled NIR spectrometer developed specifically for the characterization of singlet oxygen generation. Its main features are:

- the sample environment is a plastic integrating sphere coated with a low-atomic-number MgO reflective paint, designed to minimize shielding of the X-ray beam from the linear accelerator while generating the cascade of secondary particles that build-up the dose at the sample position;
- the integrating sphere is equipped with a fiber-optic-coupled detection optics, allowing the placement of the detector outside of the Radiotherapy LINAC shielded room;
- the detector is a compact thermoelectrically cooled InGaAs Single Photon Avalanche Photodiode module, ensuring an ideal compromise between high sensitivity and transportability.

Spectrometers employing detectors based on silicon technology, similar in design to the one proposed here, have been used to characterize the X-ray triggered luminescence emission in the UV-Vis range (XEOL) of XPDT nanoparticles (NP), such as porphyrin-functionalized mesoporous silica NP [24,25]. The proposed spectrometer aims at establishing a direct, quantitative link between 6MeV irradiated dose on the nanostructures, the concentration of $^1O_2$ and, in perspective, the cytotoxic effects on cancer cell lines.

In the following: a simplified theoretical framework of the photogeneration of $^1O_2$ in PS solutions is briefly detailed; then, the Materials and Methods section details the different components of the spectrometer, the chemical used, the methodologies of the steady-state calibration measurements and of the time-resolved experiments; finally, the results of these measurements are presented and discussed.

2. Theory

2.1. Detection of singlet oxygen by measuring the emission of its radiative deactivation

Background: we quantify photogenerated $^1O_2$ via its spontaneous radiative decay. On one hand this is the ideal approach, as the measurement does not affect nor it bypasses any other channel of molecular deexcitation, which generally are the biologically relevant ones. On the other hand, this means that the signal is intrinsically weak because it involves an optically forbidden transition from $^1O_2$ to the triplet ground state $^3O_2$.

Figure 1 reports a simplified Jablonski diagram that illustrates the process of $^1O_2$ photogeneration. The absorption of a photon (Abs, green arrow) excites the PS from its ground state S_0 to its singlet excited state S_1. Direct relaxation to S_0 might occur via fluorescence emission (Fl, orange arrow). However, a transition to a more stable triplet excited state T_1 might occur through an intersystem crossing process (ISC, undulating arrow). T_1 might decay to S_0 either via phosphorescence emission (Ph, red arrow), or through reactions such as Type II reactions with the triplet ground state of molecular oxygen $^3O_2$ (blue arrows), leading to the photogeneration of $^1O_2$.

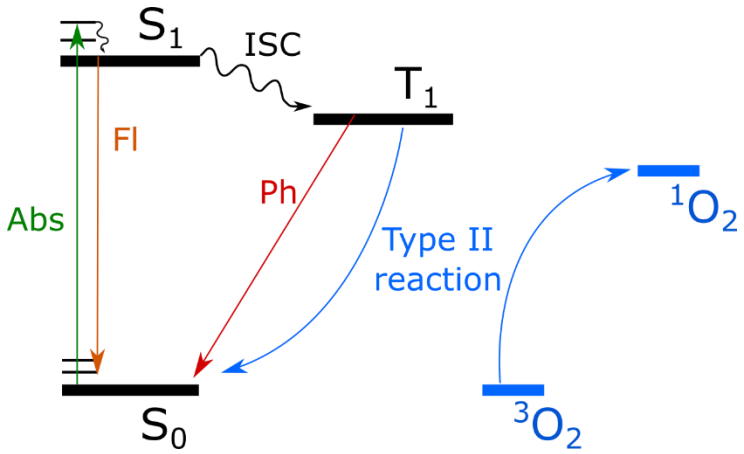

Figure 1 Simplified Jablonski diagram that illustrates the process of $^1O_2$ photogeneration. The absorption of a photon (Abs, green arrow) excites the PS from its ground state S_0 to its singlet excited state S_1. Direct relaxation to S_0 might occur via fluorescence emission (Fl, orange arrow). However, a transition to a more stable triplet excited state T_1 might occur through an intersystem crossing process (ISC, undulating arrow). T_1 might decay to S_0 either via phosphorescence emission (Ph, red arrow), or through reactions such as Type II reactions with the triplet ground state of molecular oxygen $^3O_2$ (blue arrows), leading to the photogeneration of $^1O_2$.

The relevant quantities in the description of these processes are the time-dependent concentration of PS molecules in the ground state $[S_0]$, in the excited singlet $[S_1]$ and triplet $[T_1]$ states, and of oxygen molecules in singlet excited state $[\,^1O_2\,]$. Here and in the following, [...] indicates concentration, expressed in molecules per m^3.

These concentrations are linked by differential equations [26] describing the process of photogeneration and decay of the different species

$$\frac{d[S_1]}{dt} + \frac{[S_1]}{\tau_s} = \phi\sigma_0[S_0]$$

$$\frac{d[T_1]}{dt} + \frac{[T_1]}{\tau_T} = \frac{\Phi_T[S_1]}{\tau_s}$$

$$\frac{d[\,^1O_2\,]}{dt} + \frac{[\,^1O_2\,]}{\tau_\Delta} = \frac{\Phi_\Delta[T_1]}{\Phi_T\tau_T} \qquad (1)$$

where ϕ is the incident fluence rate (in $\frac{ph}{m^2 s}$), σ_0 is the absorption cross section of the PS in its ground state (in m^2), Φ_T is the quantum yield of intersystem crossing process from the PS's singlet excited state S_1 to its triplet excited state T_1, Φ_Δ is the quantum yield of $^1O_2$ generation, τ_s is the singlet state lifetime, τ_T is the triplet state lifetime, and τ_Δ is $^1O_2$ lifetime, all in seconds.

τ_Δ is directly linked to the dominant decay channel, which depends on the molecular environment. In absence of $^1O_2$ quenchers and for dilute PS solutions, the main channel is electronic-to-vibrational energy transfer to vibrational modes of a solvent molecule, as shown by Hurst and Schuster [27,28]. This is a non-radiative channel, whose rate precisely depends on the solvent vibrational modes, however it is typically several orders of magnitude faster than the radiative channel of emission of a NIR photon with $\lambda = 1270\ nm$, which is optically forbidden because it violates spin conservation.

The value of τ_Δ is determined chiefly by the fastest decay channel. For the case of water, relevant to this study, the electronic-to-vibrational channel has $\tau_{e-v}^{\Delta} = 3.09\ \mu s$, while the radiative channel is 6 orders of magnitude slower, $\tau_{rad}^{\Delta} = 4.78\ s$ [27]. This also indicates that, in water, less than 1 in 10^6 $^1O_2$ molecules decay emitting a NIR photon; a consequence, as already stated in the beginning of this section, of the spin-forbidden $^1O_2 \rightarrow {}^3O_2$ radiative transition. Since the singlet-triplet transition of molecular oxygen in solution is dominated by electronic-to-vibrational energy transfer to solvent molecules, τ_Δ is well-known to heavily depend on the solvent chemical composition [27,28].

In the following, the differential equations (1) are solved in the simple case of steady-state illumination, ϕ = constant. Transient time effects are ignored, as well as depletion of PS and oxygen; $[S_0]$ and $\left[\ ^3O_2\ \right]$ are considered constants:

$$[S_1] = \phi\sigma_0[S_0]\tau_s$$

$$[T_1] = \Phi_T\phi\sigma_0[S_0]\tau_T$$

yielding finally the relation

$$\left[\ ^1O_2\ \right] = \Phi_\Delta\tau_\Delta\phi\sigma_0[S_0] \qquad (2)$$

In the following, a fine calibration of the NIR spectrometer is performed by measuring the amount of $^1O_2$ generated by controlled amounts of Rose Bengal, a well-known photosensitiser whose Φ_Δ is tabulated, diluted in solvents (water, ethanol, and acetone) yielding values of τ_Δ known from the literature, and employing constant fluence illumination. In this way, a calibration factor between expected concentration of photogenerated $^1O_2$ molecules and NIR fluorescence count rate is obtained.

3. Description of the instrument

The apparatus setup is shown in Figure 2. Briefly, an integrating sphere containing the sample collects its NIR emission upon excitation with a laser/LED source. A set of bandpass filters selects the desired spectral range; light collected by a NIR fiber optics collimator is sent to a fiber-coupled InGaAs cooled detector, interfaced with a PC. Each part is described in detail in the following paragraphs.

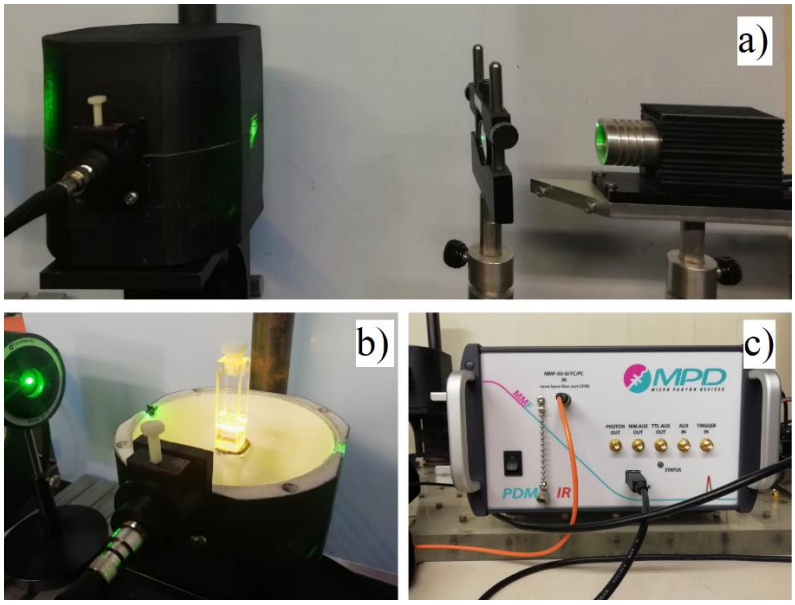

Figure 2. Spectrometer setup: a) Light from a Nd:YAG laser module passes into a narrow bandpass filter and enters into the integrating sphere via a 4mm aperture on its side. b) The opened integrating sphere, with the sample at its centre. The excitation light exits the sphere via an exit aperture. Emission light exiting the sphere on the 90° hole is filtered by a NIR bandpass filter and collected by a fiber optic collimator. c) Emission light is carried to the fiber coupled InGaAs detector module by Micro Photon Devices Srl.

Sources

A $532\ nm$ Nd:YAG laser module (LSR532ML, Lasever Inc.) is used to excite Rose Bengal; a bandpass filter ($532 \pm 3\ nm$, Brightline FF01-532/3-25, Semrock Inc.) is used to clean the laser emission. A UVC LED (3939 UVC LED from LG electronics) with emission peaked at $270\ nm$ is used to excite ZnO NP (see Section 4); it is powered by a current-limited DC power supply and it is equipped with an aluminium dissipator with a 5V brushless fan. The power output of the sources is varied either using a set of neutral filters ranging from 10 to 90% transmission, or two crossed polarizers; it is measured using a power meter (FM FieldMaster, Coherent Inc.) equipped with an optical sensor head, operating in the appropriate UV-Vis range.

Laser light incident on the quartz cuvette is partially reflected from the quartz wall; the fraction of transmitted beam entering the sample, and hence the incident fluence rate, is calculated accordingly to Fresnel's formula for the transmittance across a thick slab, using tabulated values of the refractive index of air n_0, quartz n_q and solvents n_s:

$$T = 1 - \frac{r_{0q} + r_{qw}}{1 + r_{0q} \cdot r_{qw}} \quad r_{ij} = \left(\frac{n_i - n_j}{n_i + n_j}\right)^2$$

The fraction of transmitted beam is 96.2% for water solutions in a quartz cuvette, and 96.4% for both acetone and ethanol solutions in a quartz cuvette.

Integrating sphere

The customized integrating sphere was produced by additive manufacturing, employing the so-called fused deposition modelling (FDM) 3D printing technique. As material, polylactic acid (PLA) has been selected because of its small X-ray scattering cross-section; the sphere was printed using a commercial printer (i3 Duplicator – Wanhao). The sphere is designed and printed in two halves; the top half can be removed to insert the sample. The cuvette holder, a plastic column, is designed as a separate piece and glued to the bottom half of the sphere. After the print, all pieces are sanded with sandpaper and coated with a standard spray primer, to favour adhesion of the reflective coating.

A custom-made diffuse reflectance coating is realized as follows: $2.5\ g$ of MgO powder is dissolved in $5\ mL$ Ethanol-water 1:1 mixture by mixing; $125\ mg$ of polyvinyl acetate (PVA) is added to the solution. The mixture is placed in ultrasonication bath for 10 minutes. The resulting reflective paint is used to coat the inside of the two halves of the integrating sphere, and the surface of the cuvette holder; all parts are placed in an oven at 50°C overnight. Two layers of paint are applied following the same procedure; the final surface is treated with ultrafine sandpaper (P1200 grit sandpaper). Lambertian reflectance of this coating in the range $400 - 2000\ nm$ has been checked against a UV-VIS-NIR Varian 2390 spectrometer equipped with a $BaSO_4$ coated diffuse reflectance accessory. The performances of the coating have been found to be at least as good as those in the commercial instrument.

The integrating sphere enables the accurate measurement of the fraction of incidence light absorbed by nanostructure suspension, where diffuse scattering is not negligible and impedes absorbance measurements using a standard UV-Vis spectrometer. To this aim, it can be equipped with a photodiode on one of its lateral ports; the absorbance is obtained by comparing the photodiode signal measured when a NP suspension is in the sphere with that from a solvent-filled cuvette. This procedure is reported in detail as Supplementary Information.

Light collection

Fluorescence emission from the sample exits the integrating sphere from an aperture (radius 4 mm) placed at 90° with respect to the laser aperture. A filter holder, 3D printed in PLA, holds a $0.5\ in$ bandpass filter in front of the aperture. Three bandpass filters (Edmund Optics) have been chosen to discriminate the $^1O_2$ fluorescence emission from the background: $1225 \pm 50\ nm$ (87851 FILTER BP 1275NM X 50NM OD4 12.5MM), $1275 \pm 50\ nm$ (87852), $1325 \pm 50\ nm$ (87853). A fiber optic collimator ($0.55\ Na, 1310\ nm$, Edmund Optics) collects the signal into a $1310\ nm$ multimode fiber (Thorlabs), which is connected to the detector.

Detector

The detector is a solid-state InGaAs Single Photon Avalanche Photodiodes module from Micro Photon Devices Srl [29]. This photon counting module is coupled with a multimode pigtail fiber and equipped with triple-stage Peltier cooling down to 235K. The module includes programmable electronics to control the bias voltage, the gating of the detector, the avalanche current quenching; it is equipped with USB interface for communicating with a PC through a standalone Software or a complete Software development kit. TTL outputs of detector gate signal and photon avalanches are available, enabling time-resolved experiments. In all experiments, an excess reverse bias of $2\ V$ was used, resulting in a photon detection efficiency of 14% in the wavelength range $1200 - 1500\ nm$.

4. Materials

4.1. Chemicals

Rose Bengal (CAS 632-69-9, 95% purity) to be used as a standard for reference was purchased from Sigma Aldrich; Zinc Acetate dihydrate (CAS 5970-45-6, analytical grade) was purchased from Carlo Erba Reagents; Potassium hydroxide in pellets (CAS 1310-58-3, KOH) was purchased from Merck KGaA. All chemicals were used without further purification. Air was bubbled for 30 minutes in all solvents, to equilibrate the oxygen concentration according to Henry's law; this is necessary to avoid oxygen depletion effects during $^1O_2$ generation.

4.2. ZnO nanoparticles

ZnO NP were synthetized following a sol-gel synthesis route in ethanol performed at low temperature, a modified version of the synthesis reported in [30]. Briefly, zinc acetate dihydrate (2 mmol) was dispersed in $10\ mL$ ethanol. The solution was placed in a 20 mL beaker and heated to $65\ °C$ while stirring at $400\ rpm$. After temperature stabilization, $10\ mL$ KOH ethanol solution $0.35\ M$ were added in the beaker. The white precipitate was left cooling while stirring for 30 minutes, then collected by centrifugation and washed in ethanol. The suspension was centrifuged at $2000\ g$ for $8\ min$, to remove the fraction of larger particles; the supernatant was concentrated by centrifugation at $13000\ RPM$ for 10 min and then dried in an oven at $45\ °C$ overnight.

The resulting ZnO NP have been characterized in ref [31]. Their size distribution have average diameter $49\ nm$ with standard deviation of $17\ nm$; their ζ-potential is $+53 \pm 3\ mV$. A suspension with concentration $[ZnO] = 100\ \mu g/mL$ in water was prepared and put in a quartz cuvette, sealed by a Teflon cap; the cuvette was placed into the integrating sphere. Illumination was provided by a high-power LED at $270\ nm$ (see Section 3, Sources). Measurements were performed as in the calibration experiment.

5. Methods

5.1 Calibration

The intensity of NIR emission at 1270nm observed in solutions of Rose Bengal (RB) in different solvents has been measured. The detector was operated with a hold-off time of $120\mu s$ to eliminate afterpulses. Counts are accumulated for a typical duration of 180 sec; the average count rate is corrected to account for the fraction of time the detector was switched off.

The rate R_{exc} of excitation of RB, i.e. the number of RB molecules excited each second by the beam, is determined from experimental parameters as

$$R_{exc} = \frac{P_{laser}}{h\nu}(1 - 10^{-A}) \tag{3}$$

where $(1 - 10^{-A})$ is the fraction of absorbed light by the PS solution and P_{laser} is the laser output power as measured by a standard power meter.

The investigated solutions are listed in Table 1, along with the tabulated values of Φ_Δ and τ_Δ, the excitation light's wavelength, the measured absorbance A of the sample at that wavelength. The absorption coefficient was measured on a solution with concentration 10 times higher than the one used in the photosensitizing experiments. Having always operated at concentrations well below $100\ \mu M$, we exclude effects on the absorption and fluorescence spectra due to RB aggregates in solution [32].

Solvent	Φ_Δ	$\tau_\Delta\ (\mu s)$	A @ λ_{exc}
acetone	0.70 [33]	46.5 ± 2 [34]	0.076
ethanol	0.76 [35]	16 [36]	0.089
ultrapure water	0.76 [35]	3.09 ± 0.06 [37]	0.076

Table 1 Rose Bengal (RB) solutions used to calibrate the instrument. For each solvent, the table reports the RB's $^1O_2$ quantum yield Φ_Δ, $^1O_2$ lifetime τ_Δ in the solvent, and finally the absorbance A at the excitation wavelength of the sample at the concentration $c = 4\ \mu M$. A is solvent dependent due to photochromic effects.

The number of steady-state singlet oxygen molecules is then estimated by combining eq. 2 and 3:

$$\mathrm{N}_{^1O_2} = \frac{P_{laser}}{h\nu}(1 - 10^{-A})\,\Phi_\Delta \tau_\Delta \qquad (4)$$

where P_{laser} is the light power output as measured by the power meter, and $h\nu$ is the photon energy.

For relation (4) to hold, the assumption that $[\,^3O_2\,]$ is constant over time must be verified, checking that photogeneration of $[\,^1O_2\,]$ does not cause significant depletion of $^3O_2$ in the scattering volume. To verify this, the number of dissolved O_2 molecules N_{O_2} within the scattering volume is estimated from the oxygen solubility x_{O_2} in the different air-saturated solvents, as calculated from values reported in the literature. We assume here that only O_2 molecules within the volume illuminated by the laser beam are excited to $^1O_2$, not considering effects due to possible convection. N_{O_2} is calculated from x_{O_2} as:

$$N_{O_2} = x_{O_2} N_a\, V_{exc} \qquad (5)$$

where N_a is Avogadro's number and V_{exc} is the excitation volume. The obtained values are reported in Table 2, and compared with $N_{^1O_2}$ for the Rose Bengal solutions of Table 1 illuminated by $532\ nm$ laser light at a fluence rate $\phi = 5.5 \cdot 10^{22}\,\frac{ph}{m^2\,s}$, corresponding to a power output of $70\ mW$, the maximum value used in these experiments.

Solvent	$x_{O_2}\ (mol/L)$	N_{O_2}	$N_{^1O_2}$ @ $5.5 \cdot 10^{22}\,\frac{ph}{m^2 s}$	$N_{^1O_2}/N_{O_2}\ (ppm)$
acetone [38]	$2.5 \cdot 10^{-3}$	$4.67 \cdot 10^{16}$	$9.9 \cdot 10^{11}$	21
ethanol [38]	$2.1 \cdot 10^{-3}$	$3.88 \cdot 10^{16}$	$4.3 \cdot 10^{11}$	11
ultrapure water [39,40]	$0.26 \cdot 10^{-3}$	$4.85 \cdot 10^{15}$	$0.7 \cdot 10^{11}$	1.4

Table 2. Fraction of oxygen converted to its singlet state. First column is the oxygen solubilities x_{O_2} in solvents (in mol/L), as obtained from the literature for $T = 298\ K$ and $PP_{O_2} = 0.21\ atm$ partial pressure of oxygen; the number N_{O_2} of oxygen molecules dissolved in the excitation volume, calculated according to eq. (5); the number $N_{^1O_2}$ of $^1O_2$ molecules generated illuminating the samples by $532\ nm$ light at a fluence rate of $5.5 \cdot 10^{22}\,\frac{ph}{m^2 s}$ calculated according to eq. (4). From these values, the relative concentration $N_{^1O_2}/N_{O_2}$ is obtained; the low concentrations estimated at high illumination power exclude oxygen depletion effects.

In the cases considered, the estimated fraction of photogenerated $^1O_2$ is a few ppm with respect to the total amount of dissolved O_2; depletion effects are therefore excluded. The effect of possible convective motion would increase N_{O_2} within the excitation volume, thus making this figure even smaller.

To compare the measurement performed in different solvents, an additional factor has to be included in the analysis: the different absorption of NIR photons by the solvents. While acetone is transparent to NIR photons in the $1200 - 1350\ nm$ region, ethanol and particularly water presents significant absorbance.

The NIR intensities, after subtraction of background counts, can be corrected to account for absorption by the solvent by multiplication by a factor $r_{NIR} = 10^{kL}$, where k is the extinction coefficient of the solvent in the spectral interval of each filter, and L is the average length of the path of a NIR photon across the solvent. A quantitative, analytical calculus of L is a very complex task, that would have to take into account the initial path from the point of generation of the photon within the sample to the side of the cuvette, as well as all possible successive intersection of the photon path with the cuvette volume following a reflection from the integrating sphere walls. As a qualitative estimate, we assume that L is of the same order of magnitude of the lateral size of the sample. Therefore, we assume $L = 1\ cm$, the lateral size of the cuvette. Average extinction coefficients κ are obtained by averaging over the relevant spectra window $1250 \leq \lambda \leq 1300\ nm$ from absorbance data obtained using a Varian UV-VIS-NIR spectrophotometer; the results are listed in Table 3.

Solvent	$\boldsymbol{k\ (cm^{-1})}$ $1250 \leq \lambda \leq 1300\ nm$
acetone	0.023
ethanol	0.127
ultrapure water	0.437

Table 3: average extinction coefficient of solvents in the spectral intervals of the NIR filter corresponding to $^1O_2$ phosphorescence emission.

6. Results

6.1. Calibration: steady state detection

In this section, we report on $^1O_2$ detection measurements on the known PS Rose Bengal. Figure 3 reports, for the three NIR bandpass filters, the count rate measured under $2.1 \cdot 10^{22} \frac{ph}{m^2 s}$ illumination at $532\ nm$ on three different samples: ultrapure water (black squares), used to measure the background counts; a water solution of $[RB] = 16\ \mu M$ (white circles); an analogous RB aqueous solution containing also a quencher of RB's triplet excited state, $[KI] = 300\ mM$ (yellow diamonds). In the latter, ions provide an efficient non-radiative deexcitation route for the PS, thus suppressing $^1O_2$ generation.

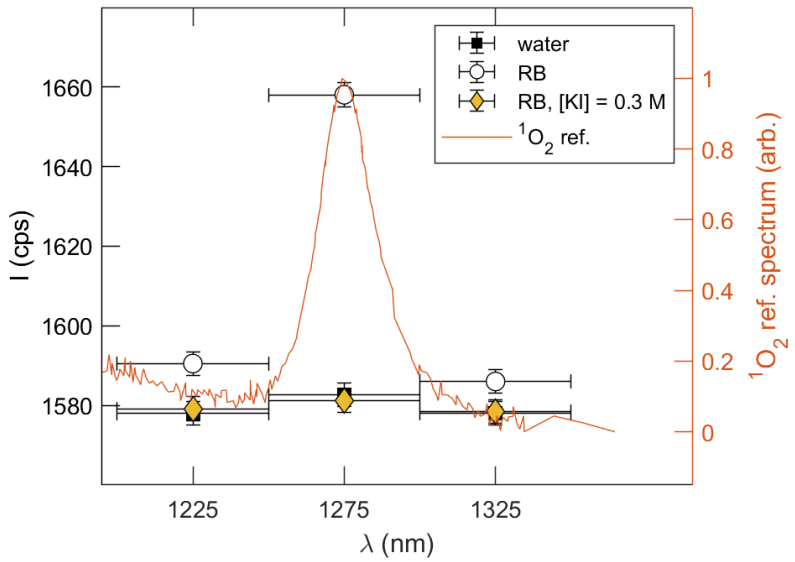

Figure 3. Near Infrared count rate measured under constant illumination (532 nm, 27 mW) on three samples; ultrapure water (black squares) used to characterize the background signal; a water solution of $[RB] = 16\mu M$ (white circles); an analogous RB aqueous solution containing also a quencher of RB's triplet excited state, $[KI] = 300\ mM$ (yellow diamonds). Results are compared with a normalized spectrum of $^1O_2$ emission from the literature (orange line, left axis) [41].

The measurement on the RB solution (white) shows a maximum when the $1275\ nm$ filter is used, i.e. in correspondence of the emission peak corresponding to the radiative transition of molecular oxygen from singlet to triplet state. When the quencher of RB's triplet state is introduced, background count rates are observed. The measurements are compared with the emission spectrum of $^1O_2$ in this wavelength range, as obtained from the literature (orange line) [41] .

Experiments of $^1O_2$ detection under continuous constant-power illumination for the three samples listed in Table 1, performed as detailed in section 3, are reported in Figure 4. The background subtracted NIR count rate, scaled to account for the different NIR absorption coefficient of the three solvents, is reported as a function of the rate R_{exc} of excitation of Rose Bengal, i.e. the number of PS molecules excited each second by the beam within the scattering volume, as obtained from eq. (3). The higher counts observed in acetone and ethanol reflect the lower non-radiative de-excitation rate of $^1O_2$ in these solvents, with respect to that observed in water

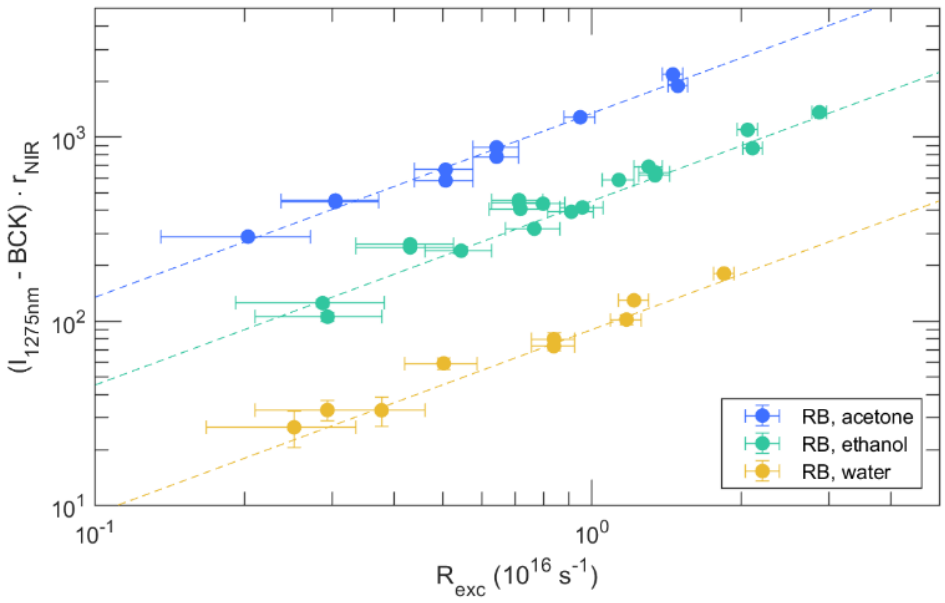

Figure 4 Measurement performed on Rose Bengal solutions in different solvents (see Table 1). The background subtracted NIR count rate, scaled to account for the different NIR absorption coefficient of the three solvents, is reported as a function of the number of Rose Bengal molecules excited per second (R_{exc}). The higher counts observed in acetone and ethanol reflect the lower non-radiative de-excitation rate of $^1O_2$ in these solvents, with respect to that observed in water. Lines are linear trends with zero intercept to guide the eye.

6.2. Singlet oxygen generation by ZnO nanoparticles

Figure 5 reports on the left axis the background subtracted NIR intensity, corrected for absorption by water, as a function of the rate of absorbed UV photons by the ZnO NP, determined from the UV LED output power and from the fraction F_{abs} of incident photons absorbed by the NP suspension. The latter is measured using the integrating sphere, which allows to measure the absorbance taking into account the non-negligible diffuse scattering by the ZnO NP (see the complete procedure detailed as Supplementary Information), finding $F_{abs} = 0.75 \pm 0.02$.

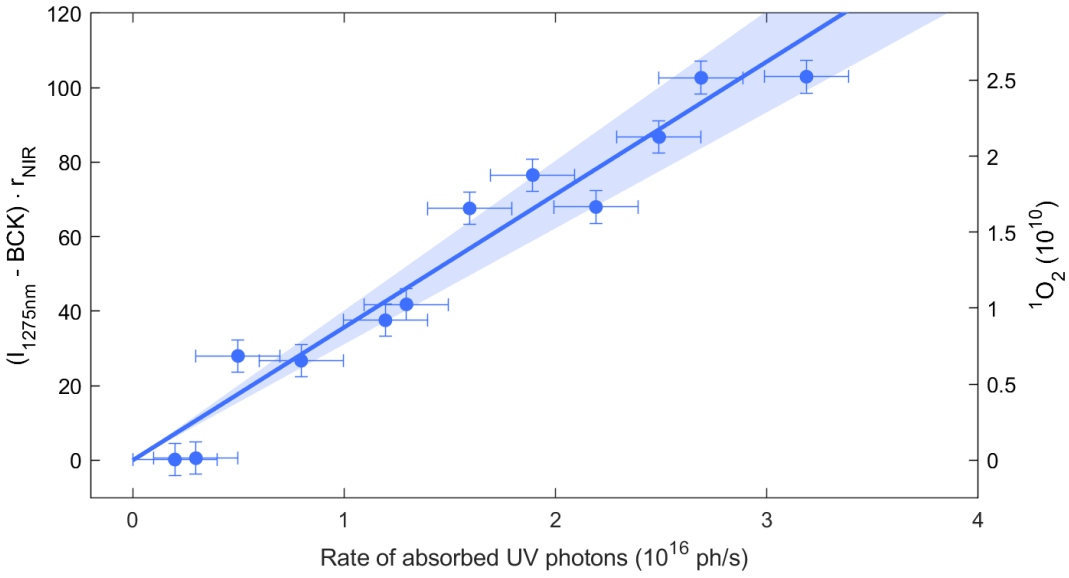

Figure 5. NIR emission measurement on a ZnO suspension in water. Left axis: background subtracted NIR count rate, scaled to account for NIR absorption coefficient in water, as a function of the estimated number of absorbed UV photons per seconds. Right axis: corresponding number of generated $^1O_2$ moieties, calculated from the Rose Bengal calibration factor f_{cal} (see Section 7, eqn. 6). The line is a fit to the linear trend of eq. (4), from which the $^1O_2$ quantum yield of the ZnO NP is estimated to be $\Phi_\Delta = 0.28 \pm 0.04$ (see Section 7 for discussion). The blue-coloured area reflects the uncertainty over Φ_Δ as determined by the fitting procedure.

7. Discussion

Data shown of Figure 4 collapse on a single curve when the abscissa reports the steady-state number of $^1O_2$ molecules $N_{^1O_2}$, calculated as in eq. (4) as $N_{^1O_2} = R_{exc}\Phi_\Delta\tau_\Delta$; rescaled results are reported in Figure 6. By means of a linear fit of the data, we obtain a calibration value of

$$f_{cal} = (2.45 \pm 0.09) \cdot 10^8 \quad (6)$$

$^1O_2$ molecules per rescaled NIR count-per-second at 1275nm in the scattering volume.

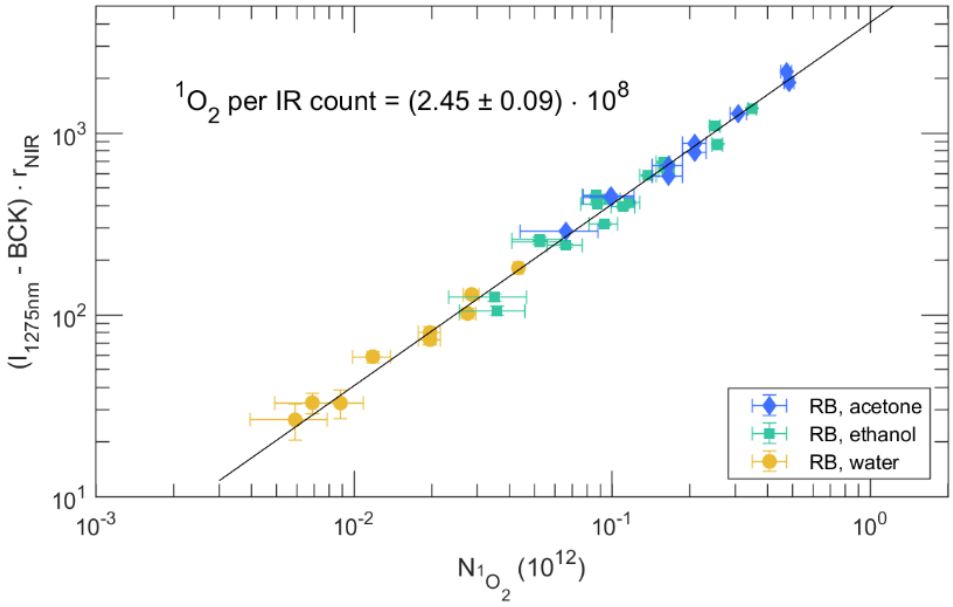

Figure 6. The data of Figure 4 collapse on a single calibration master curve when reported as a function of the expected number of steady-state $^1O_2$ molecules generated in solution $N_{^1O_2}$. $N_{^1O_2}$ is determined using equation (4). Literature values of Rose Bengal's $^1O_2$ quantum yield Φ_Δ and of the lifetime τ_Δ of $^1O_2$ in the solvent are used (see Table 1). By means of a linear fit, we obtain a calibration value of $(2.45 \pm 0.09) \cdot 10^8$ *$^1O_2$ molecules per NIR count-per-second at 1275nm.*

In water, the minimum detected NIR signal during a 180 second acquisition was 20 ± 5 counts. It was observed under experimental conditions corresponding to $N_{^1O_2} \sim 5 \cdot 10^9$. This value, compared to the total number of oxygen molecules in water within the excitation volume $N_{^3O_2} \sim 5 \cdot 10^{15}$ (see section 5, Table 2), corresponds to a relative $^1O_2$ concentration of $\sim 1\ p.p.m.$

A detection threshold as a function of the acquisition time is obtained considering the uncertainty of the background counts in dark. Assuming standard Poissonian statistics, we define the detection threshold TH as the value of $N_{^1O_2}$ that corresponds to a NIR count rate that differs from the background by $3\sigma_b$, where σ_b is the standard deviation of the background counts $b(t_{int})$ detected within the integration time t_{int}:

$$\mathrm{TH} = \min\left(N_{^1O_2}\right) = 3\sigma_b \cdot f_{cal} = 3\sqrt{b(t_{int})} \cdot f_{cal} \quad (7)$$

Relation 7 is inverted to calculate the integration time needed to reach the desired sensitivity; results, calculated from the background count rate reported in Figure 3, are reported in Figure 7. The detection threshold ranges from $TH = 4 \cdot 10^9$ $^1O_2$ molecules – attained with an integration time of $\sim 1\ min$ – down to $TH = 10^9$ $^1O_2$ reached with a $\sim 14\ min$ integration time. Assuming a detection experiment under an X-ray beam, where a typical sample volume of 2 mL is uniformly illuminated by the excitation beam, those values corresponds to a minimum detectable $^1O_2$ molar concentration from $3.3\ pM$ at $14\ min$ integration time, to $0.83\ pM$ at $1\ min$.

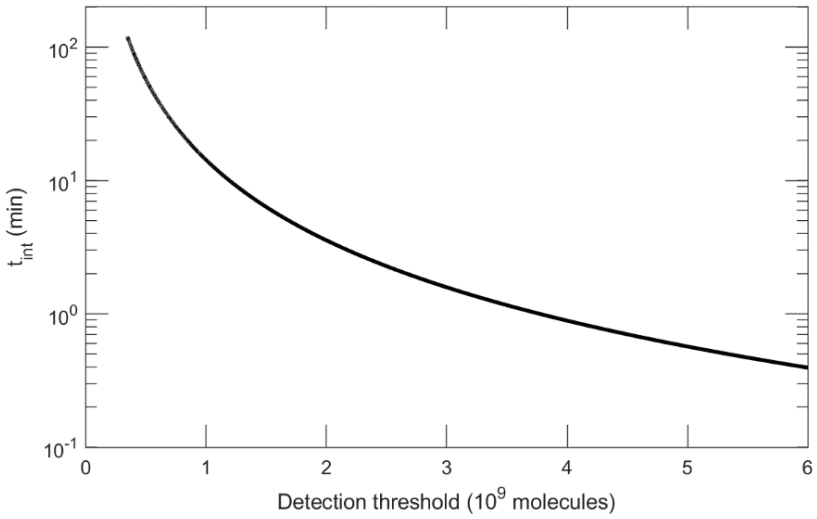

Figure 7: Integration time necessary to achieve specific values of detection threshold TH, i.e. the minimum number of detectable $^1O_2$ molecules, calculated accordingly to eq. (7).

It is worth comparing this detection threshold with that of a state-of-the-art chemofluorescent probes for $^1O_2$ detection, nanoaggregates of tethraphenylethylene-phthalhydrazid (NTPE-PH), a selective $^1O_2$ probe that can operate in aqueous solution, *in vitro* cell cultures, as well as *in vivo* [9,42]*;* a detection threshold concentration $c_{TH} = 4.9\,nM$ is reported. While the NIR spectrometer can reach a much lower $^1O_2$ detection threshold, it is worth recalling that those values are valid only in water solution, assuming negligible diffuse scattering and negligible NIR absorption from the PS moiety. During *In vitro* and *in vivo* experiments, the $^1O_2$ lifetime is typically several orders of magnitude lower than in pure water, significantly reducing the sensitivity of $^1O_2$ direct detection by NIR spectroscopy.

Having calibrated the instrument using Rose Bengal, we test its use to characterize the performances of ZnO NP. These are widely investigated for PDT, photodegradation of chemicals and antibacterial treatments, because of the high ROS quantum yield observed under irradiation from UV lamps as well as under natural illumination [43]. In recent years many papers explored the application of ZnO NP as PS in nanostructures for PDT in deep tissue, by coupling them to scintillating NP [31,44–46], quantum dots [47], or metal NP [43]. These are excited by a penetrating radiation (X-rays, NIR photons), activating ZnO in cascade.

ROS generation pathways in semiconductor nanostructures such as ZnO NP are different than those of standard molecular photosensitizers. The promotion of an electron to the conduction band, e.g. by the absorption of a photon with energy higher than the band-gap, results in an electron-vacance pair than can interact with water and oxygen via several different pathways to generate ROS, mainly superoxide and hydroxyl radicals [43,48], as well as $^1O_2$ [49]. Surface defects, in particular oxygen vacancies, increase the amount of photogenerated ROS [50], determining also the relative weight of these pathways [51,52]. As a consequence of this, the morphology and size of the ZnO nanoparticle severely affects the ROS generation [53], the relative fraction of each ROS produced and the resulting photo-oxidative stress on cells and bacteria.

Therefore, Φ_Δ is not a characteristic of the material, rather of the specific nanostructure. In this respect, a rapid assay to determine Φ_Δ would be a precious tool to guide NP development towards better PDT performances. So far, standard chemofluorescent assays fail to this task in the case of ZnO NP.

For instance, 1,3-Diphenylisobenzofuran (DPBF) is a non-specific chemofluorescent probe that interacts with $^1O_2$ and hydroxyl radicals; the ROS-induced quenching of the fluorescence is proportional to the amount of

photogenerated ROS, and the ROS quantum yield is derived by comparison with known photosensitizers. DPBF effectiveness as a probe is limited by autooxidation, imposing strict protocols of control measurements that increase the experiment complexity [54]. DPBF was used to determine the ROS quantum yield of ZnO NP and Ag-doped ZnO NP, finding respectively $\Phi_{\mathrm{ROS}} = 0.13$ and $\Phi_{\mathrm{ROS}} = 0.28$ [55]. ROS generation was only indirectly categorised as 77–83% $^1O_2$ and 18–27% hydroxyl radical by means of ROS scavenger assays on cells, which are not suited for a rapid NP prototyping strategy.

SOSG also been applied to determine Φ_Δ of ZnO NP, despite the known problem that SOSG itself might generate $^1O_2$ under irradiation with the UV light used to trigger ZnO photoactivity. SOSG experiments on small (<10nm) ZnO NP have reported as high as $\Phi_\Delta = 0.66$ [56]. SOSG experiments performed on ZnO NP associated with alloyed $CuInZn_xS_{2+x}$ quantum dots found $\Phi_\Delta = 0.248$ [47]. SOSG was also used by the authors to determine Φ_Δ for CeF_3-ZnO nanostructures with size in the range $100 - 300\ nm$ irradiated with $254\ nm$ UV light. In these nanostructures, scintillating CeF_3 NP decorate a ZnO nanostructure; CeF_3 efficiently absorbs high energy X-rays to excite ZnO in cascade, in a realization of XPDT; however, CeF_3 absorption bands in the UV range enhance the photoactivity of the nanostructures also in the wavelength range. The authors found $\Phi_\Delta = 0.35 \pm 0.03$ [44,45].

The instrument proposed in this paper fulfils the need for a simpler, direct, and quantitative approach to the determination of Φ_Δ, which then could be used to guide and improve the synthesis of ZnO nanostructures towards enhanced PDT performances. Moreover, the measurement is performed without the addition of any chemical to the suspension, which might adsorb to the nanoparticle surface and limit $^1O_2$ generation or alter the colloidal stability of the suspension. This is exemplified in the measurement reported in Figure 5. The right axis reports the steady-state number of $^1O_2$ molecules $\mathrm{N}_{^1O_2}$, obtained by applying the calibration factor f_{cal} to the background subtracted NIR intensity, as a function of the estimated number of absorbed UV photons per seconds. Data are fitted to a linear trend by means of a least-squares algorithm; the angular coefficient of the regression line is the product $\Phi_\Delta \cdot \tau_\Delta$. The uncertainty over the angular coefficient is obtained considering the dominating uncertainty, i.e. the one over the rate of absorbed UV photons.

Assuming the literature value $\tau_\Delta = 3.09\mu s$ for water (see Table 1), the $^1O_2$ quantum yield of the ZnO NP determined by the measurement is

$$\Phi_\Delta^{\mathrm{ZnO}} = 0.28 \pm 0.04.$$

The value measured is consistent with those previously reported for NP nanoparticles with size larger than 50 nm. The large relative uncertainty ($\sim 15\ \%$) in the determination of $\Phi_\Delta^{\mathrm{ZnO}}$ is mainly due to the low precision of the measurement of the incident fluence rate of UV light; this aspect will be a challenge also in the investigation of X-ray irradiated PDT nanostructures, where the X-ray dose released within the sample has to be evaluated by numerical simulations.

8. Conclusions

We designed and developed a portable NIR spectrometer for the direct, quantitative detection of $^1O_2$. It is based on a fiber-coupled, thermoelectrically cooled InGaAs Single Photon Avalanche Photodiode developed by Micro Photon Devices (MPD Srl), coupled to an integrating sphere. The spectrometer response was calibrated against the standard PS Rose Bengal diluted in different solvents and excited by means of a $532\ nm$ solid state green laser.

The instrument is capable of detecting $^1O_2$ concentrations below $1\ p.p.m.$ with respect to the total amount of oxygen in air-saturated water at ambient temperature; a 2 minutes integration time results in a detection

threshold of $\sim 2.5\ pM$ in a uniformly irradiated 2 mL PS water solution. The instrument was used to determine the $^1O_2$ quantum yield $\Phi_\Delta^{\mathrm{ZnO}}$ of ZnO nanostructures irradiated by UV light at $270\ nm$; this is, to our knowledge, the first application of quantitative direct $^1O_2$ detection to UV-irradiated PDT nanostructured, an experimental condition that would normally be particularly challenging for detection with standard chemofluorescent probes.

This instrument is suited to characterize nanostructures that aim to apply Photodynamic Therapy to the treatment of tumours in deep tissues, where standard PDT irradiation cannot reach. These nanostructures generate reactive oxygen species when triggered by highly penetrating radiation, such as X-rays from Radiotherapy Linear Accelerator [17–19] or Near-Infrared light from solid-state lasers and LEDs [12–16]. The lack of a spectrometer specifically designed to quantify $^1O_2$ generation from these nanostructures has so far hindered their development.

In a future work, using this instrument we plan to demonstrate for the first time the possibility of directly linking the amount of $^1O_2$ generated by X-PDT nanostructures to the X-ray dose released in the sample.

As Appendix I, we report a preliminary evaluation of the performances of the apparatus for time-resolved measurements of the lifetime of $^1O_2$.

Acknowledgment

D.O. acknowledges financial support by the programme “FIL-Quota Incentivante” of University of Parma, co-sponsored by Fondazione Cariparma. The authors acknowledge Micro Photon Devices Srl, in particular A. Giudice and G. Simmerle, for the cooperation in the development of this instrument through its NIR detector, and useful discussion on its operation. D.O. acknowledge prof. C. Viappiani (University of Parma) for useful discussion and insight on TCSPC experiments.

Appendix I: Time-resolved detection capabilities

After the calibration under steady state illumination, we characterize the performances of the apparatus in TCSPC experiments. The detector electronics allows for accurate timing of the photon pulses, eliminating the need for additional signal processing electronics; using a compact, low-cost Time-to-digital TDC-GP22 acquisition board (Acam-messelectronic GmbH) it is possible to perform singlet oxygen lifetime measurements using a gated acquisition scheme (full details are available as Supplementary Information).

Experiments were performed on RB solutions ($[RB] = 8\ \mu M$) in ethanol (blue) and acetone (red); the laser beam is modulated in pulses with duration $200\mu s$ and period $500\mu s$. Results a reported in Figure 8, left panel. Experiments were also performed on RB aqueous solution ($[RB] = 16\ \mu M$), with laser pulses of duration $20\mu s$ and period $40\mu s$. Results are reported in the right panel of Figure 9.

Curves were fitted with a convolution of the exponential decay with the curve $I_L(t)$ acquired by measuring le laser light impinging on the frosted side of an absorption quartz cuvette (black symbols in the figure):

$$I(t) = \int_0^T I_L(s)\, H(t-s) \exp\left(-\frac{t-s}{\tau_\Delta}\right) ds \qquad (8)$$

where $H(t)$ is the Heaviside step function and T the period of the laser pulses. Fitting was performed using the *fMINUIT* minimization tool, a suite of minimization tools ported from MINUIT to MATLAB by G. Allodi [57] . Results of the fitting are reported in Table 4.

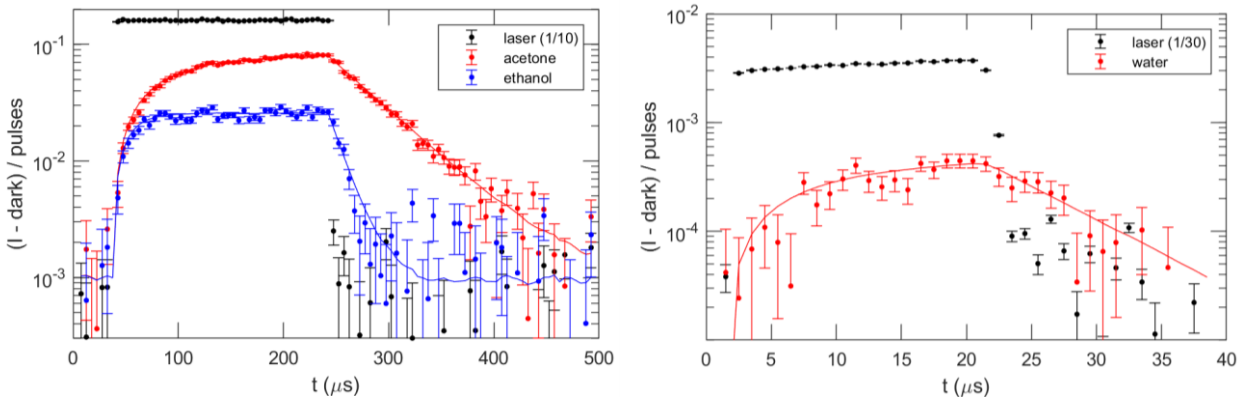

Figure 8 Left: TCSPC measurements performed on Rose Bengal solutions, $[RB] = 8\ \mu M$ in acetone (red) and ethanol (blue), obtained with an integration time of 2 h. Right: TCSPC measurements performed on Rose Bengal solutions, $[RB] = 16\ \mu M$ in water (red), with integration time of 6 hours. The solid line is a fit to the convolution of an exponential decay with the measurement of scattered laser light (eq. 8, black points).

Solvent	$\tau_\Delta\ (\mu s)$
acetone	53 ± 5
ethanol	16 ± 7
water	7 ± 5

Table 4. Results of fitting the TCSPC curves of Figure 9 using the model of eq. (8).

The measurements evidence a limited accuracy of the instrument, in particular in experiments performed on aqueous samples; this is mainly due to the high background count rates of InGaAs detectors. In typical TCSPC experiments, avoiding pile-up and hold-off time effects require working with a low number of counts per pulse ($cpp \ll 1$). To measure relaxation times of the order of the tens of microseconds, such as singlet oxygen lifetimes in water, a laser repetition rate of the order of $1 - 25\ KHz$ is needed. This value is of the same order of magnitude as the background count rate $b \sim 1580\ cps$ (see Figure 3); therefore, these experiments is characterized by $cpp \sim 1$. In this condition, the photon detection probability decays exponentially with the

pulse-count delay time t, complicating the analysis (see Supplementary information). The condition $cpp \ll 1$ have been restored by employing the aforementioned gated acquisition scheme (Supplementary Information); however, this scheme requires very long acquisition times, of the order of several hours, to reach a sufficient signal to noise ratio.

Bibliography

[1] S.A. Castaldo, J.R. Freitas, N.V. Conchinha, P.A. Madureira, The Tumorigenic Roles of the Cellular REDOX Regulatory Systems, Oxid. Med. Cell. Longev. 2016 (2016) 1–17. https://doi.org/10.1155/2016/8413032.

[2] D. Trachootham, J. Alexandre, P. Huang, Targeting cancer cells by ROS-mediated mechanisms: A radical therapeutic approach?, Nat. Rev. Drug Discov. 8 (2009) 579–591. https://doi.org/10.1038/nrd2803.

[3] H. Pelicano, D. Carney, P. Huang, ROS stress in cancer cells and therapeutic implications, Drug Resist. Updat. 7 (2004) 97–110. https://doi.org/10.1016/j.drup.2004.01.004.

[4] C.S. Foote, Definition of type I and type II photosensitized oxidation., Photochem. Photobiol. 54 (1991) 659. https://doi.org/10.1111/j.1751-1097.1991.tb02071.x.

[5] A.P. Castano, T.N. Demidova, M.R. Hamblin, Mechanisms in photodynamic therapy: Part one - Photosensitizers, photochemistry and cellular localization, Photodiagnosis Photodyn. Ther. 1 (2004) 279–293. https://doi.org/10.1016/S1572-1000(05)00007-4.

[6] R. Bonnett, Photosensitizers of the porphyrin and phthalocyanine series for photodynamic therapy, Chem. Soc. Rev. 24 (1995) 19–33. https://doi.org/10.1039/CS9952400019.

[7] M.C. DeRosa, R.J. Crutchley, Photosensitized singlet oxygen and its applications, Coord. Chem. Rev. 233–234 (2002) 351–371. https://doi.org/10.1016/S0010-8545(02)00034-6.

[8] M. Garcia-Diaz, Y.Y. Huang, M.R. Hamblin, Use of fluorescent probes for ROS to tease apart Type I and Type II photochemical pathways in photodynamic therapy, Methods. 109 (2016) 158–166. https://doi.org/10.1016/j.ymeth.2016.06.025.

[9] W. Yu, L. Zhao, Chemiluminescence detection of reactive oxygen species generation and potential environmental applications, Trends Anal. Chem. 136 (2021) 116197. https://doi.org/10.1016/j.trac.2021.116197.

[10] S. Kim, M. Fujitsuka, T. Majima, Photochemistry of singlet oxygen sensor green, J. Phys. Chem. B. 117 (2013) 13985–13992. https://doi.org/10.1021/jp406638g.

[11] S.K. Sharma, M.R. Hamblin, The Use of Fluorescent Probes to Detect ROS in Photodynamic Therapy, in: J. Espada (Ed.), React. Oxyg. Species, Humana, New York, NY, 2021: pp. 215–229. https://doi.org/10.1007/978-1-0716-0896-8_17.

[12] Q. Wang, Y. Dai, J. Xu, J. Cai, X. Niu, L. Zhang, R. Chen, Q. Shen, W. Huang, Q. Fan, All-in-One Phototheranostics: Single Laser Triggers NIR-II Fluorescence/Photoacoustic Imaging Guided Photothermal/Photodynamic/Chemo Combination Therapy, Adv. Funct. Mater. 29 (2019) 1–12. https://doi.org/10.1002/adfm.201901480.

[13] M. Wang, J. Song, F. Zhou, A.R. Hoover, C. Murray, B. Zhou, L. Wang, J. Qu, W.R. Chen, NIR-Triggered Phototherapy and Immunotherapy via an Antigen-Capturing Nanoplatform for Metastatic Cancer Treatment, Adv. Sci. 6 (2019). https://doi.org/10.1002/advs.201802157.

[14] Y. Dai, J. Su, K. Wu, W. Ma, B. Wang, M. Li, P. Sun, Q. Shen, Q. Wang, Q. Fan, Multifunctional Thermosensitive Liposomes Based on Natural Phase-Change Material: Near-Infrared Light-Triggered Drug Release and Multimodal Imaging-Guided Cancer Combination Therapy, ACS Appl. Mater. Interfaces. 11 (2019) 10540–10553. https://doi.org/10.1021/acsami.8b22748.

[15] Y. Liu, X. Meng, W. Bu, Upconversion-based photodynamic cancer therapy, Coord. Chem. Rev. 379 (2019) 82–98. https://doi.org/10.1016/j.ccr.2017.09.006.

[16] W. Fan, P. Huang, X. Chen, Overcoming the Achilles' heel of photodynamic therapy, Chem. Soc. Rev. 45 (2016) 6488–6519. https://doi.org/10.1039/C6CS00616G.

[17] W. Fan, W. Tang, J. Lau, Z. Shen, J. Xie, J. Shi, X. Chen, Breaking the Depth Dependence by

Nanotechnology-Enhanced X-Ray-Excited Deep Cancer Theranostics, Adv. Mater. 31 (2019) 1–32. https://doi.org/10.1002/adma.201806381.
[18] W. Sun, Z. Zhou, G. Pratx, X. Chen, H. Chen, Nanoscintillator-mediated X-ray induced photodynamic therapy for deep-seated tumors: From concept to biomedical applications, Theranostics. 10 (2020) 1296–1318. https://doi.org/10.7150/thno.41578.
[19] B. Cline, I. Delahunty, J. Xie, Nanoparticles to mediate X-ray-induced photodynamic therapy and Cherenkov radiation photodynamic therapy, Wiley Interdiscip. Rev. Nanomedicine Nanobiotechnology. 11 (2019) e1541. https://doi.org/10.1002/wnan.1541.
[20] F. Rossi, E. Bedogni, F. Bigi, T. Rimoldi, L. Cristofolini, S. Pinelli, R. Alinovi, M. Negri, S.C. Dhanabalan, G. Attolini, F. Fabbri, M. Goldoni, A. Mutti, G. Benecchi, C. Ghetti, S. Iannotta, G. Salviati, Porphyrin conjugated SiC/SiOx nanowires for X-ray-excited photodynamic therapy, Sci. Rep. 5 (2015) 1–6. https://doi.org/10.1038/srep07606.
[21] X. Ragàs, A. Jiménez-Banzo, D. Sánchez-García, X. Batllori, S. Nonell, Singlet oxygen photosensitisation by the fluorescent probe Singlet Oxygen Sensor Green®, Chem. Commun. (2009) 2920. https://doi.org/10.1039/b822776d.
[22] H. Liu, P.J.H. Carter, A.C. Laan, R. Eelkema, A.G. Denkova, Singlet Oxygen Sensor Green is not a Suitable Probe for 1O2 in the Presence of Ionizing Radiation, Sci. Rep. 9 (2019) 1–8. https://doi.org/10.1038/s41598-019-44880-2.
[23] A.-L. Bulin, C. Truillet, R. Chouikrat, F. Lux, C. Frochot, D. Amans, G. Ledoux, O. Tillement, P. Perriat, M. Barberi-Heyob, C. Dujardin, X-ray-Induced Singlet Oxygen Activation with Nanoscintillator-Coupled Porphyrins, J. Phys. Chem. C. 117 (2013). https://doi.org/10.1021/jp4077189.
[24] A. Vejdani Noghreiyan, M.R. Sazegar, S.A. Mousavi Shaegh, A. Sazgarnia, Investigation of the emission spectra and cytotoxicity of TiO2 and Ti-MSN/PpIX nanoparticles to induce photodynamic effects using X-ray, Photodiagnosis Photodyn. Ther. 30 (2020) 101770. https://doi.org/10.1016/j.pdpdt.2020.101770.
[25] A. Darafsheh, S. Najmr, T. Paik, M.E. Tenuto, C.B. Murray, J.C. Finlay, J.S. Friedberg, Characterization of rare-earth-doped nanophosphors for photodynamic therapy excited by clinical ionizing radiation beams, Opt. Methods Tumor Treat. Detect. Mech. Tech. Photodyn. Ther. XXIV. 9308 (2015) 930812. https://doi.org/10.1117/12.2079373.
[26] M.S. Patterson, S.J. Madsen, B.C. Wilson, Experimental tests of the feasibility of singlet oxygen luminescence monitoring in vivo during photodynamic therapy., J. Photochem. Photobiol. B. 5 (1990) 69–84. https://doi.org/10.1016/1011-1344(90)85006-i.
[27] C. Schweitzer, R. Schmidt, Physical mechanisms of generation and deactivation of singlet oxygen, Chem. Rev. 103 (2003) 1685–1757. https://doi.org/10.1021/cr010371d.
[28] J.R. Hurst, G.B. Schuster, Nonradiative Relaxation of Singlet Oxygen in Solution, J. Am. Chem. Soc. 105 (1983) 5756–5760. https://doi.org/10.1021/ja00356a009.
[29] A. Tosi, A. Della Frera, A. Bahgat Shehata, C. Scarcella, Fully programmable single-photon detection module for InGaAs/InP single-photon avalanche diodes with clean and sub-nanosecond gating transitions, Rev. Sci. Instrum. 83 (2012) 013104. https://doi.org/10.1063/1.3675579.
[30] D. Sun, M. Wong, L. Sun, Y. Li, N. Miyatake, H.J. Sue, Purification and stabilization of colloidal ZnO nanoparticles in methanol, J. Sol-Gel Sci. Technol. 43 (2007) 237–243. https://doi.org/10.1007/s10971-007-1569-z.
[31] D. Orsi, D. Bernardi, G. Giovanardi, F. Rossi, K. Szczepanowicz, L. Cristofolini, Rationale design of a layer-by-layer nanostructure for X-ray induced photodynamic therapy, Colloid Interface Sci. Commun. 39 (2020) 100327. https://doi.org/10.1016/j.colcom.2020.100327.
[32] D. Xu, D.C. Neckers, Aggregation of rose bengal molecules in solution, J. Photochem. Photobiol. A Chem. 40 (1987) 361–370. https://doi.org/10.1016/1010-6030(87)85013-X.
[33] P. Gottschalk, J. Paczkowski, D.C. Neckers, Factors influencing the quantum yields for rose bengal formation of singlet oxygen, J. Photochem. 35 (1986) 277–281. https://doi.org/10.1016/0047-2670(86)87059-9.
[34] P.R. Ogilby, C.S. Foote, Chemistry of Singlet Oxygen. 42. Effect of Solvent, Solvent Isotopic Substitution, and Temperature on the Lifetime of Singlet Molecular Oxygen (1δg), J. Am. Chem. Soc. 105 (1983) 3423–3430. https://doi.org/10.1021/ja00349a007.

[35] M.A.J. Rodgers, P.T. Snowden, Lifetime of O2(1Δg) in Liquid Water As Determined by Time-Resolved Infrared Luminescence Measurements, J. Am. Chem. Soc. 104 (1982) 5541–5543. https://doi.org/10.1021/ja00384a070.
[36] F. Wilkinson, J.G. Brummer, Rate constants for the decay and reactions of the lowest electronically excited singlet state of molecular oxygen in solution, J. Phys. Chem. Ref. Data. 10 (1981) 809–999. https://doi.org/10.1063/1.555655.
[37] S.Y. Egorov, V.F. Kamalov, N.I. Koroteev, A.A. Krasnovsky, B.N. Toleutaev, S. V. Zinukov, Rise and decay kinetics of photosensitized singlet oxygen luminescence in water. Measurements with nanosecond time-correlated single photon counting technique, Chem. Phys. Lett. 163 (1989) 421–424. https://doi.org/10.1016/0009-2614(89)85161-9.
[38] T. Sato, Y. Hamada, M. Sumikawa, S. Araki, H. Yamamoto, Solubility of oxygen in organic solvents and calculation of the Hansen solubility parameters of oxygen, Ind. Eng. Chem. Res. 53 (2014) 19331–19337. https://doi.org/10.1021/ie502386t.
[39] G.A. Truesdale, A.L. Downing, G.F. Lowden, The solubility of oxygen in pure water and sea-water, J. Appl. Chem. 5 (2007) 53–62. https://doi.org/10.1002/jctb.5010050201.
[40] W. Xing, M. Yin, Q. Lv, Y. Hu, C. Liu, J. Zhang, Oxygen Solubility, Diffusion Coefficient, and Solution Viscosity, Elsevier B.V., 2014. https://doi.org/10.1016/B978-0-444-63278-4.00001-X.
[41] M. Scholz, R. Dědic, J. Valenta, T. Breitenbach, J. Hála, Real-time luminescence microspectroscopy monitoring of singlet oxygen in individual cells, Photochem. Photobiol. Sci. 13 (2014) 1203–1212. https://doi.org/10.1039/C4PP00121D.
[42] S. Zhang, H. Cui, M. Gu, N. Zhao, M. Cheng, J. Lv, Real-Time Mapping of Ultratrace Singlet Oxygen in Rat during Acute and Chronic Inflammations via a Chemiluminescent Nanosensor, Small. 15 (2019) 1–9. https://doi.org/10.1002/smll.201804662.
[43] C. Yi, Z. Yu, Q. Ren, X. Liu, Y. Wang, X. Sun, S. Yin, J. Pan, X. Huang, Nanoscale ZnO-based photosensitizers for photodynamic therapy, Photodiagnosis Photodyn. Ther. 30 (2020) 101694. https://doi.org/10.1016/j.pdpdt.2020.101694.
[44] T. Rimoldi, D. Orsi, P. Lagonegro, B. Ghezzi, C. Galli, F. Rossi, G. Salviati, L. Cristofolini, CeF3-ZnO scintillating nanocomposite for self-lighted photodynamic therapy of cancer, J. Mater. Sci. Mater. Med. 27 (2016) 159.
[45] D. Orsi, T. Rimoldi, S. Pinelli, R. Alinovi, M. Goldoni, G. Benecchi, F. Rossi, L. Cristofolini, New CeF3-ZnO nanocomposites for self-lighted photodynamic therapy that block adenocarcinoma cell life cycle, Nanomedicine. 13 (2018) 2311–2326. https://doi.org/10.2217/nnm-2017-0399.
[46] S. Sahi, W. Chen, Luminescence enhancement in CeF3/ZnO nanocomposites for radiation detection, Radiat. Meas. 59 (2013). https://doi.org/10.1016/j.radmeas.2013.04.015.
[47] F. Donat, S. Corbel, H. Alem, S. Pontvianne, L. Balan, G. Medjahdi, R. Schneider, ZnO nanoparticles sensitized by CuInZnxS2+x quantum dots as highly efficient solar light driven photocatalysts, Beilstein J. Nanotechnol. 8 (2017) 1080–1093. https://doi.org/10.3762/bjnano.8.110.
[48] P. Sivakumar, M. Lee, Y.S. Kim, M.S. Shim, Photo-triggered antibacterial and anticancer activities of zinc oxide nanoparticles, J. Mater. Chem. B. 6 (2018) 4852–4871. https://doi.org/10.1039/c8tb00948a.
[49] Y. Yamamoto, N. Imai, R. Mashima, R. Konaka, M. Inoue, W.C. Dunlap, Singlet oxygen from irradiated titanium dioxide and zinc oxide., Methods Enzymol. 319 (2000) 29–37. https://doi.org/10.1016/s0076-6879(00)19005-6.
[50] J. Singh, S. Juneja, S. Palsaniya, A.K. Manna, R.K. Soni, J. Bhattacharya, Evidence of oxygen defects mediated enhanced photocatalytic and antibacterial performance of ZnO nanorods, Colloids Surfaces B Biointerfaces. 184 (2019) 110541. https://doi.org/10.1016/j.colsurfb.2019.110541.
[51] V. Lakshmi Prasanna, R. Vijayaraghavan, Insight into the Mechanism of Antibacterial Activity of ZnO: Surface Defects Mediated Reactive Oxygen Species even in the Dark, Langmuir. 31 (2015) [1] K. A. Alim, V. A. Fonoberov, M. Shamsa, and A. https://doi.org/10.1021/acs.langmuir.5b02266.
[52] R. Kumar, A. Umar, G. Kumar, H.S. Nalwa, Antimicrobial properties of ZnO nanomaterials: A review, Ceram. Int. 43 (2017) 3940–3961. https://doi.org/10.1016/j.ceramint.2016.12.062.
[53] Q. ul A. Naqvi, A. Kanwal, S. Qaseem, M. Naeem, S.R. Ali, M. Shaffique, M. Maqbool, Size-dependent inhibition of bacterial growth by chemically engineered spherical ZnO nanoparticles, J. Biol. Phys. 45

(2019) 147–159. https://doi.org/10.1007/s10867-019-9520-4.
[54] J.A. Howard, G.D. Mendenhall, Autoxidation and Photooxidation of 1,3-Diphenylisobenzofuran: A Kinetic and Product Study, Can. J. Chem. 53 (1975) 2199–2201. https://doi.org/10.1139/v75-307.
[55] A. Nadhman, S. Nazir, M. Ihsanullah Khan, S. Arooj, M. Bakhtiar, G. Shahnaz, M. Yasinzai, PEGylated silver doped zinc oxide nanoparticles as novel photosensitizers for photodynamic therapy against Leishmania, Free Radic. Biol. Med. 77 (2014) 230–238. https://doi.org/10.1016/j.freeradbiomed.2014.09.005.
[56] S.L.P. Luengas, G.H. Marin, L. Rivera, A. Tarditti, G. Roque, E. Mansilla, Zinc Oxide Nanoparticles and Photodynamic Therapy for the Treatment of B-chronic Lymphocytic Leukemia, Leuk. - Updat. New Insights. (2015). https://doi.org/10.5772/61796.
[57] G. Allodi, FMINUIT, a MATLAB multidimensional nonlinear minimization by means of the MINUIT engine, (2010). https://www.fis.unipr.it/~giuseppe.allodi/Fminuit/Fminuit_intro.html

Supplementary Information of the article

A portable NIR spectrometer directly quantifies singlet oxygen generated by nanostructures for Photodynamic Therapy.

Orsi Davide[1], Vaccari Marco[1], Baraldi Andrea[1], Cristofolini Luigi[1]

[1] - Università di Parma, Dipartimento di Scienze Matematiche, Fisiche e Informatiche, Parma (IT)

Time-resolved acquisition in gated-mode

Time-Correlated Single Photon Counting (TCSPC) experiments were performed to test the sensitivity of the apparatus with respect to measurements of singlet oxygen lifetime in different solvents. As mentioned in Section 3, the detector electronics allows for accurate timing of the photon pulses, eliminating the need for additional signal processing electronics; using a compact Time-to-digital conversion board (TDC-GP22, Acam-messelectronic GmbH) it is possible to perform singlet oxygen lifetime measurements using a gated acquisition scheme. The board, developed for ultrasonic ranging, is capable of measuring time delays in the range $500\ ns - 4\ ms$ with a resolution of $22\ ps$, and thus suitable for the measurements the fluorescence lifetime of singlet oxygen.

TCSPC experiments to measure the lifetime of singlet oxygen must overcome the problem in term of signal-to-noise ratio. In typical TCSPC experiments, to avoid pile-up and hold-off time effects, it is required to work with a number of counts per laser pulse $cpp \ll 1$. To measure relaxation times of the order of tens of microseconds, such as singlet oxygen lifetimes, a laser repetition rate of $1 - 25\ KHz$ is needed. These values are comparable to the background count rate of state-of-the-art InGaAs SPAD such as the one used in this paper, about 10^3.

In this paper, to overcome this problem, we exploit the fast control electronics of the SPAD detector, operating in gated mode, by applying its excess bias for a small fraction of time at a very high repetition rate. In this way, the condition $cpp \ll 1$ can be fulfilled.

The 532nm laser is operated at 30mW output power. The laser beam is modulated by an Acousto-optic modulator (NEC 0D-8813A, acoustic frequency $140\ MHz$); the first order diffraction peak is selected and used to excite Rose Bengal solutions in different solvents. The modulation consists in a sequence of 40 pulses of duration $2.5\ \mu s$ and period $5\ \mu s$; the pulse train has therefore a total duration of $200\ \mu s$. The repetition rate of the pulse train is $2\ kHz$. The detector is operated in gated mode, controlled by a TTL signal of frequency $200\ kHz$ synchronized with the fast laser pulses. Every TTL pulse, the detector is turned on for $1\ \mu s$, i.e. for 20% of the gate period. If a count (either a real photon or a dark count pulse) is detected within this window, the detector is turned off for $500\ \mu s$ (e.g. hold-off time), i.e. a full period of the laser operation.

The TTL output signal from the detector is fed to the Start input of the Time-to-digital conversion (TDC) board; the stop signal is given by the laser TTL signal that indicates the start of the next train of laser pulses. The TDC is interfaced with a PC via an Arduino UNO microcontroller.

The TTL signals used in TCSPC experiments and the effects of the gated operation mode on dark counts are exemplified in Figure S1.

The top panels reports the TTL signals: from top to bottom, it shows a) the pulses used to modulate the laser beam; b) the pulses used to turn on the SPAD detector; c) a sample pulse indicating the detection of a dark count / NIR photon, used to start the time-to-digital conversion; and d) the stop signal, i.e. the convolution of the laser pulse train, used to stop the time-to-digital conversion.

The bottom panel reports TSCPC measurements performed in dark, with the lased blocked by a beam stop, with the detector operating in free-running mode (orange) and in the gated mode here described (blue). In free-running mode, with $120\mu s$ holdoff time, the count rate was $\sim 1580\ cps$; in gated mode, the count rate was $\sim 300\ cps$, 15% of the laser repetition rate ($2\ kHz$). The gated acquisition correctly shows equal probability of detection in each time bin, as expected for an acquisition of dark counts. On the contrary, the free-running signal shows a non-flat curve, caused by the very high count rate ($cpp \sim 1$) and by the long dead time ($120\mu s$) of the detector necessary to supress after-pulsing.

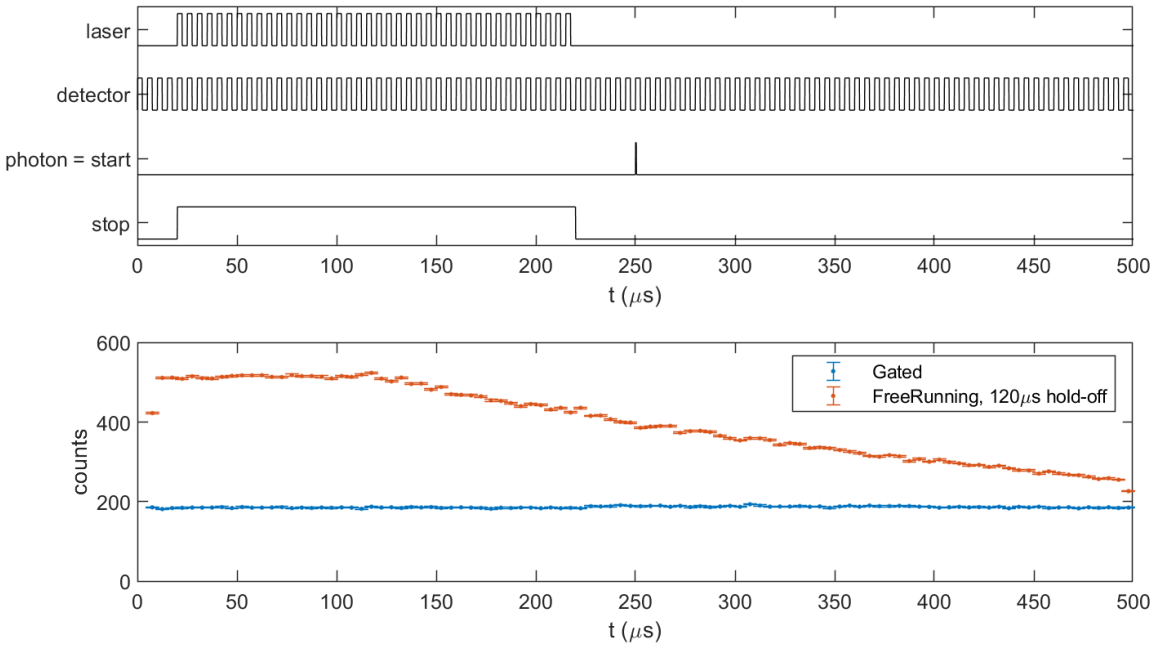

Figure S1 ***TOP:*** *TTL signal of the TCSPC experiment; the laser emits sequences of fast pulses, repeated every $500\mu s$, while the detector is turned on at 200kHz repetition rate, synchronized with the detector fast pulses. The detection of a photon triggers the time-to-digital measurement of the pulse-photon delay, which is stopped by the start of the next train of laser pulses.* ***BOTTOM:*** *acquisition in dark, with the detector operating in free-running mode (orange) and in gated mode (blue). Gated operation ensures that every time bin has equal detection probability.*

Measuring the fraction of absorbed UV light in ZnO nanoparticle suspension

The integrating sphere enables the accurate measurement of the fraction of incidence light absorbed by nanostructure suspension, where diffuse scattering is not negligible. In this case, transmittance measurements using a standard UV-Vis spectrometer do not yield accurate results.

In this work, the integrating sphere was used to measure the fraction of UV light absorbed by a ZnO nanoparticle suspension.

A side port of the sphere was equipped with a SiC photodiode, with peak sensitivity at 270 nm, operating in photovoltaic mode; the fraction of incident light absorbed by the suspension is deduced by comparing the photodiode signal measured when at the centre of the sphere there is a) a water-filled quartz cuvette and b)

the same cuvette with the NP suspension. The photodiode signal measured in these two cases at different value of the incident photon rate is reported in Figure S2.

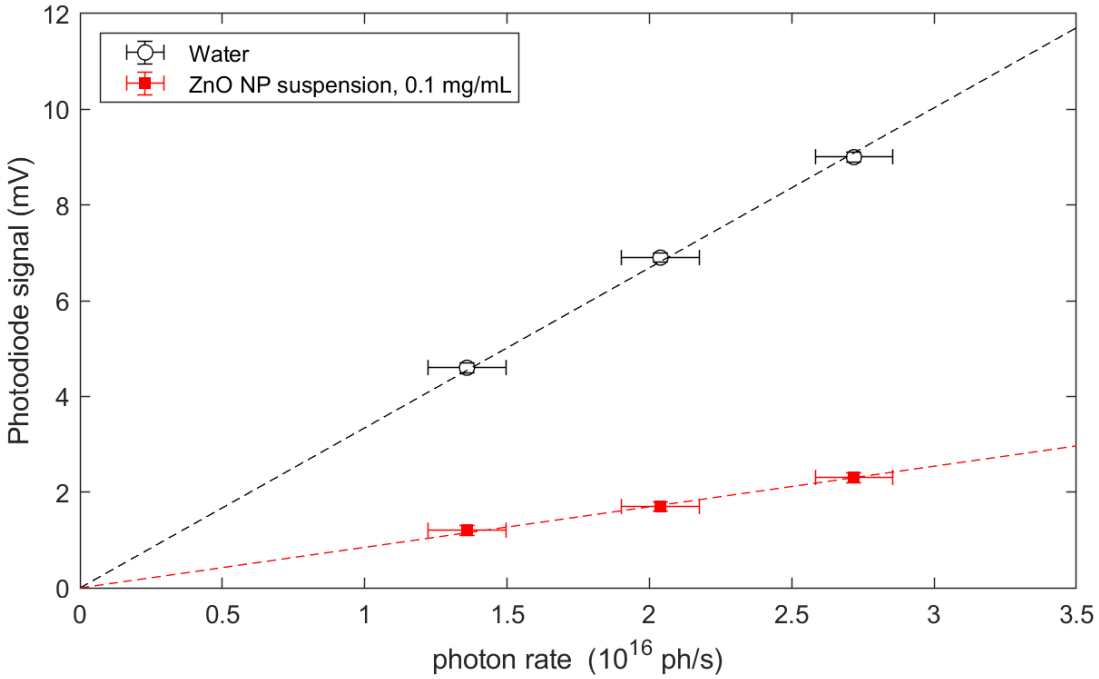

Figure S2 Signal measured by the SiC photodiode that equips the integrating sphere, measured for different values of the incident UV photon rate emitted by a 270nm UV led on two samples; a water suspension in a quartz cuvette (white circles) and the ZnO nanoparticle suspension (red circles). The signal in the latter case is lower because of ZnO absorption. Dashed line are linear fits.

For both samples, the photodiode signal shows a direct proportionality with the photon rate; the signal measured with the ZnO suspension at the centre of the sphere is lower that for a water-filled cuvette, because of UV absorption by ZnO nanoparticles.

The fraction of incident photons absorbed by ZnO nanoparticles is estimated from the angular coefficients α of linear fits $V = \alpha\phi$, as

$$F_{abs} = 1 - \frac{\alpha_{ZnO}}{\alpha_{water}}$$

The analysis yields $F_{abs} = 0.75 \pm 0.02$.

Declaration of Interest Statement

UNIVERSITÀ
DI PARMA

DIPARTIMENTO DI SCIENZE
MATEMATICHE, FISICHE
E INFORMATICHE

Parco Area delle Scienze 7/A , 43124 PARMA

A portable NIR spectrometer directly quantifies singlet oxygen generated by nanostructures for Photodynamic Therapy.

Orsi Davide[1], Vaccari Marco[1], Baraldi Andrea[1], Cristofolini Luigi[1]

[1] - Università di Parma, Dipartimento di Scienze Matematiche, Fisiche e Informatiche, Parma (IT)

Parma, 12/04/2021

Conflict of interest: NONE

On behalf of all the authors

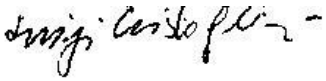

Luigi Cristofolini
Associate professor
Department of Mathematical, Physical and Computer Sciences,
University of Parma